Supporting Information:

Detection of SARS-CoV-2 with Aptamer-Modified Nanopipettes

Shekemi Denuga,[a] Dominik Duleba,[a] Pallavi Dutta,[a] Guerrino Macori,[c,d] Damion K. Corrigan,[b] Séamus Fanning, [c,e] Robert P. Johnson.[a,c]*

a) School of Chemistry, University College Dublin, Belfield, Dublin 4, Ireland.
b) Centre for Advanced Measurement Science and Health Translation, Department of Pure and Applied Chemistry, University of Strathclyde, G1 1XL
c) UCD-Centre for Food Safety, University College Dublin, Belfield, Dublin 4, Ireland.
d) School of Biology & Environmental & Biological Sciences, University College Dublin, Belfield, Dublin 4, Ireland.
e) School of Public Health, Physiotherapy & Sports Science, University College Dublin, Belfield, Dublin 4, Ireland.

*robert.johnson@ucd.ie

Contents

S1. Severe Acute Respiratory Syndrome Coronavirus 2

Figure S1 illustrates Severe acute respiratory syndrome coronavirus 2 (SARS-CoV-2), a viral pathogen characterized by a positive-sense, single-stranded ribonucleic acid (RNA) genome that is approximately 30 kbp in size.[1] Encoded within its genome are non-structural replicase polyproteins and four structural proteins: spike (S), nucleocapsid (NC), envelope (E), and membrane (M).[2, 3] The S glycoprotein consists of two functional domains: the S1 receptor-binding domain, which is responsible for recognizing and binding to the host receptor angiotensin-converting enzymes 2 (ACE2), and an S2 domain, which enables the virus to fuse with the host cell membrane.[4]

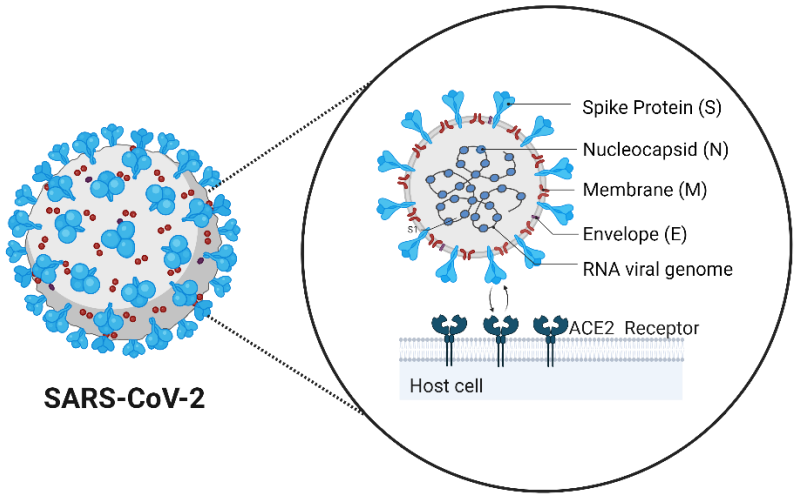

Figure S1: Illustration of the SARS-CoV-2 virus and interaction of the spike protein S1 domain with the ACE2 receptor on a host cell. Adapted from "COVID-19 virus" and "COVID-19 virus 3D" by BioRender.com (2024).

S2. Nanopipette Characterization

The radii of nanopipettes were determined by recording a current-voltage (*I-V*) curve in a 0.1 M KCl electrolyte solution (**Fig. S2**). The nanopipette was backfilled with electrolyte, and an Ag/AgCl wire working electrode was inserted into the stem. Then, the nanopipette was placed in a bulk electrolyte solution containing an Ag/AgCl wire reference electrode. The applied voltage was swept from -1 V to +1 V relative to the reference electrode at a scan rate of 0.1 V sec^{-1}. Using EC-Lab software, a linear fit was applied to the *I-V* curve, and the slope was extracted. The radius of the nanopipette is calculated using **Equation S1**, where the resistance (*R*) is the inverse of conductivity (obtained from the slope of the *I-V* curve), K is electrolyte conductivity, and θ is the half-cone angle.[5, 6]

$$r = \frac{1}{\kappa R}\left(\frac{1}{\pi \tan\theta} + \frac{1}{4}\right) \qquad \textbf{Equation S1}$$

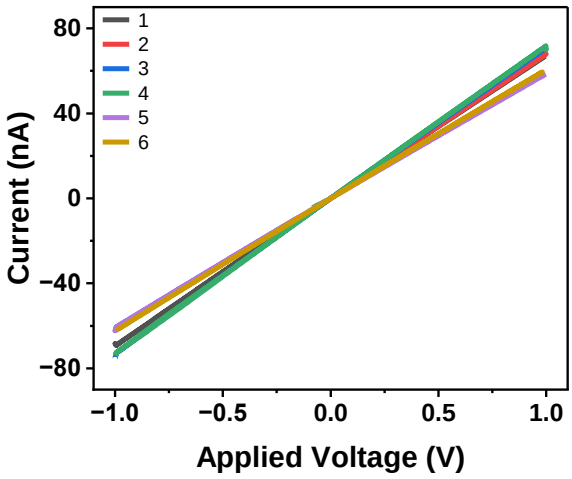

Figure S2: Current-voltage responses obtained for quartz nanopipettes with a mean radius of 109 ± 20 nm in 0.1 M KCl (n=6).

Scanning Electron Microscopy (SEM) was performed on a selected sub-set of nanopipettes to confirm the geometry and pore size (**Fig S3**). The nanopipette taper was then analyzed using ImageJ.

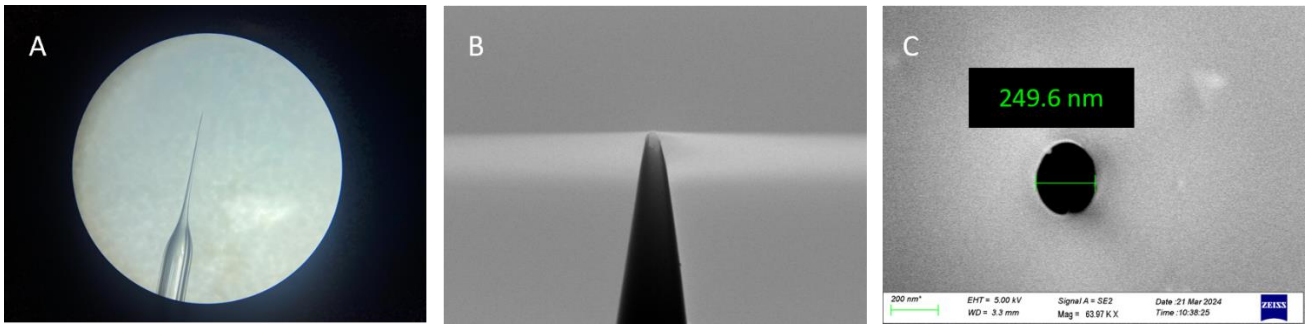

Figure S3: Characterization of quartz nanopipettes with a mean radius of 109 ± 20 nm. (A) Image taken using a smartphone by aligning it with the eyepiece of the microscopes with a 10X objective. (B) Side-view SEM of the nanopipette. (C) Top view SEM of the nanopipette.

S3. Bio-Layer Interferometry Analysis of the SARS-CoV-2 Aptamer

Biolayer Interferometry (BLI) was used to determine the affinity of the S1 aptamer for the S1 domain of SARS-CoV-2 (**Fig. S4**).[7] The aptamer exhibits high binding affinity for wild-type (WT) S1 protein and the spike protein in its trimeric state, as evidenced by dissociation constants (KD) of 10.17 ± 0.07 and 1.19 ± 0.04, respectively. The low nanomolar K_D values demonstrate the sensitivity and selectivity of the aptamer sequence's high affinity for the S1 protein. Due to the continuous evolution of SAR-CoV-2, additional BLI analyses were also carried out to evaluate the binding affinity of the aptamers towards SARS-CoV-2 variants, including the Alpha (B.1.1.7), Beta (B.1.351), and Delta (B1.1617.2) variants. The aptamer shows efficient binding to all three variants, indicating that mutations in the S1 protein do not impede the aptamer binding site. Conversely, no discernible binding is observed when the aptamer is exposed to the HCoV-NL63 virus, commonly known as the common cold (**Fig. S4**).[8]

Table S1. The affinity of the S1 aptamer to the SARS-CoV-2 S1 WT, the spike protein trimer, and the SARS-CoV-2 S1 variants was determined by BLI analysis.

Protein	K_D **(nM)**
WT SARS-CoV-2 S1	10.17 ± 0.07
SARS-CoV-2 WT spike protein trimer	1.19 ± 0.04
Delta variant S1	11.07 ± 0.1
Beta variant S1	6.71 ± 0.22
Alpha variant S1	13.50 ± 0.25
HCoV-NL63 S1 Domain	No binding determined

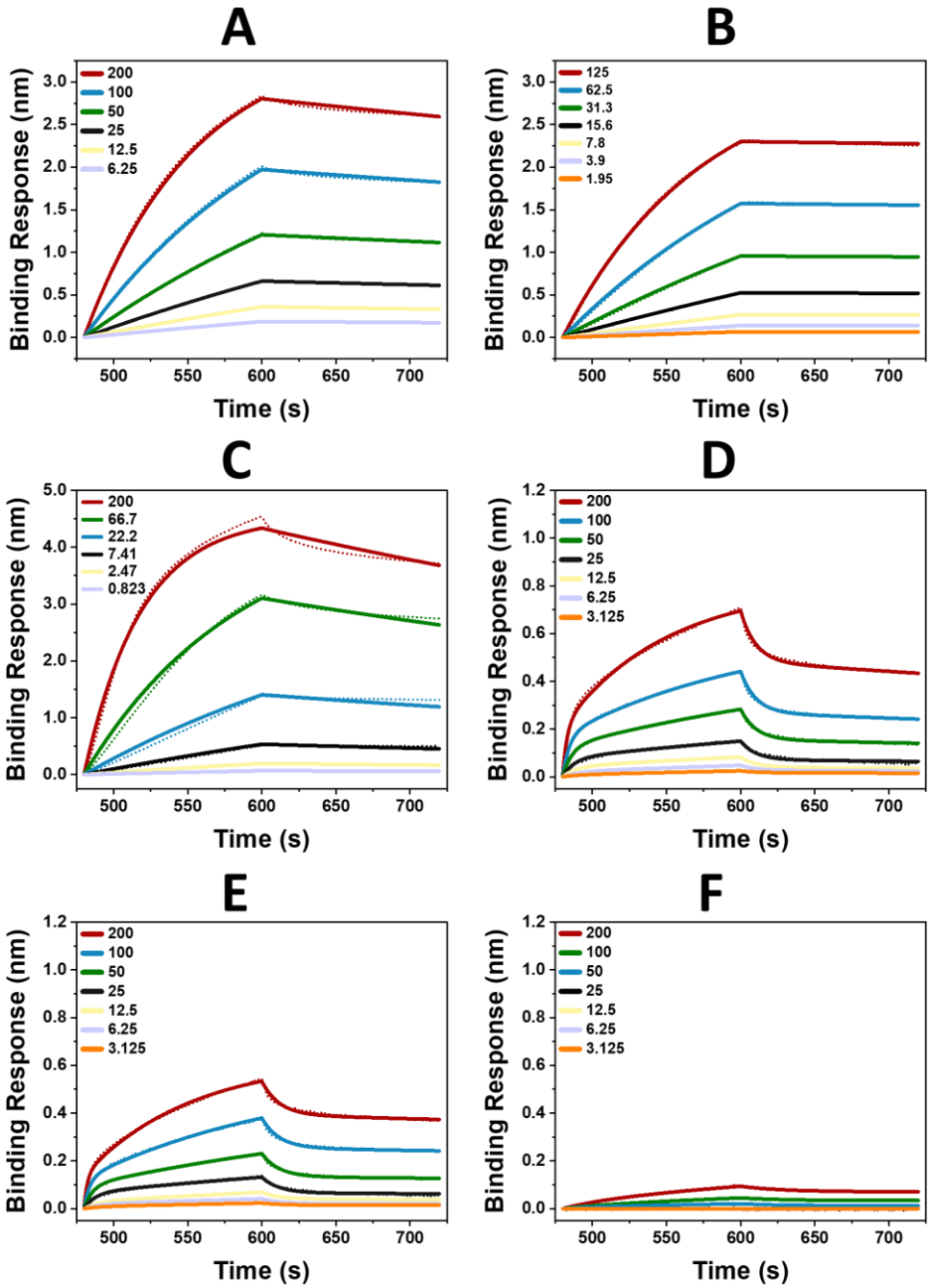

Figure S4: BLI data (dotted lines) of the SARS-CoV-2 aptamer against various concentrations of (A) WT SARS-CoV-2 S1(B) SARS-CoV-2 Spike protein trimer (C) Delta variant S1 (D) Beta variant S1 (E) Alpha variant S1 (F) Human-coronavirus NL63 S1, all fitted to a 1:1 binding model (solid lines).

S4. Finite Element Simulations

Finite Element Analysis was carried out in the commercial software COMSOL® Multiphysics 6.2, where the Nernst-Plank equation (**Equation S2**) is solved self-consistently with the Poisson equation (**Equation S3**) to obtain the concentration and potential profiles:

$$\mathrm{J}_i = -\mathrm{D}_i \nabla c_i - \frac{z_i F}{RT} D_i c_i \nabla \Phi \qquad \textbf{(Equation S2)}$$

$$\nabla^2 \Phi = -\frac{F}{\epsilon} \sum_i z_i c_i \qquad \textbf{(Equation S3)}$$

where J_i denotes the ion flux, c_i the concentration, D_i the diffusion coefficient, and z_i the charge number of the i^{th}, F is the Faraday constant, R is the ideal gas constant, T is the temperature, Φ is the electric potential, and ϵ denotes the permittivity. A nanopore with a 100 nm pore radius and 10° internal half-cone angle is used in simulations. The pipette height extends to 40 µm while the bulk solution is 5 µm (**Fig. S5 A**), both sufficiently large to allow the concentration and potential gradients to naturally resolve back to boundary values. Boundary layer elements are used on the charged surfaces, and triangular elements are used elsewhere (**Fig. S5 B**). The complete built mesh consists of 790821 domain elements and 43771 boundary elements.

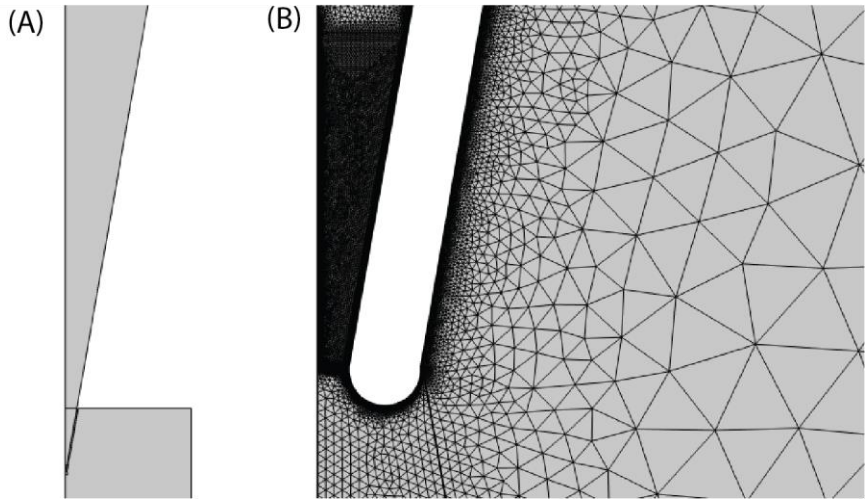

Figure S5: The nanopipette geometry used for the model, and (B) a zoomed-in view of the meshed nanopipette tip region.

The thickness of the surface modification is included in the model by decreasing the effective nanopore mouth and increasing the thickness of the walls by 32 nm to account for the APTES layer[9] and by 21.1 nm to account for the aptamer layer. The thickness contributed by the MPS crosslinker is not accounted for, as it is negligible compared to the other modifications. The nanopore surface is

assumed to possess a +5 mC m^{-2} surface charge density to account for the positively charged silane layer before aptamer immobilization. A negative surface charge density is added by assuming a 0.3×10^{12} cm^{-2} aptamer surface density, with each aptamer possessing 33 free electrons (1 free electron per phosphate unit).[10] This consideration results in the surface being net negatively charged with an even distribution of charge in the interior of the nanopore (as the aptamer is backfilled in the experiments). Exposure to the spike protein subunit is carried out by dipping the sensor in the spike subunit overnight; as such, the interior of the nanopipette will not be uniformly modified with the spike subunit. Each S1 subunit is assumed to contribute a charge of 12 free electrons,[11] and the spike subunit's contributed surface density cannot exceed that of the aptamer. The spike surface density is assumed to exponentially decay from the tip via **Equation S4**:

$$\sigma(z) = \sigma_{spike} \times e^{-\frac{z}{\tau}} + \sigma_{aptamer} \qquad \textbf{Equation S4}$$

Where $\sigma(z)$ is the surface charge density at position z, z is the distance from the nanopore mouth, σ_{spike} is the surface charge density contributed by the spike subunit, $\sigma_{aptamer}$ is the surface charge density contributed by the aptamer and τ is the factor controlling the decay rate of the exponential function. This expression yields a maximum surface charge density of $\sigma_{aptamer}$ + σ_{spike} that decays to the surface charge density of $\sigma_{aptamer}$. The rate of decay is dictated by the term τ, which is calculated based on the diffusive distance of the spike subunit during the exposure period and assumes that 90% of the exponential decay is reached at the spike diffusion distance.

$$\tau = \frac{L_D}{\ln(1 - 0.9)}$$

Where L_D is the distance the spike protein can diffuse inside the nanopore during the spike exposure time.

$$L_D = \sqrt{2D_{spike}t}$$

Where t is the spike exposure time and D_{spike} is the diffusion coefficient given by the Einstein-Stokes equations:

$$D_{spike} = \frac{k_B T}{6\pi\eta R}$$

Where k_B is the Boltzmann constant, T is the temperature, η is the dynamic viscosity of the solvent, and R is the radius of the spike subunit.

The finite element method was employed to simulate *I-V* curves for each functionalization step and the binding of the S1 domain to the aptamer. As observed experimentally, the positively rectifying APTES-modified nanopipette became negatively rectifying following aptamer immobilization on the nanopore surface (**Fig S6 A**). Moreover, the binding of the S1 subunit to the aptamer also gave rise to increased negative rectification. This result was further analyzed computationally by mapping the normalized ionic enrichment (defined as the average concentration of potassium and chloride divided by the bulk electrolyte concentration) along the central axis (z) of the nanopipette. From this, we could deduce that the enhanced rectification observed following aptamer-S1 binding was due to increased ion enrichment at negative potentials and more drastic ion depletion at positive potential (particularly at the pore tip) as the surface becomes more negatively charged (**Fig S6 B**).

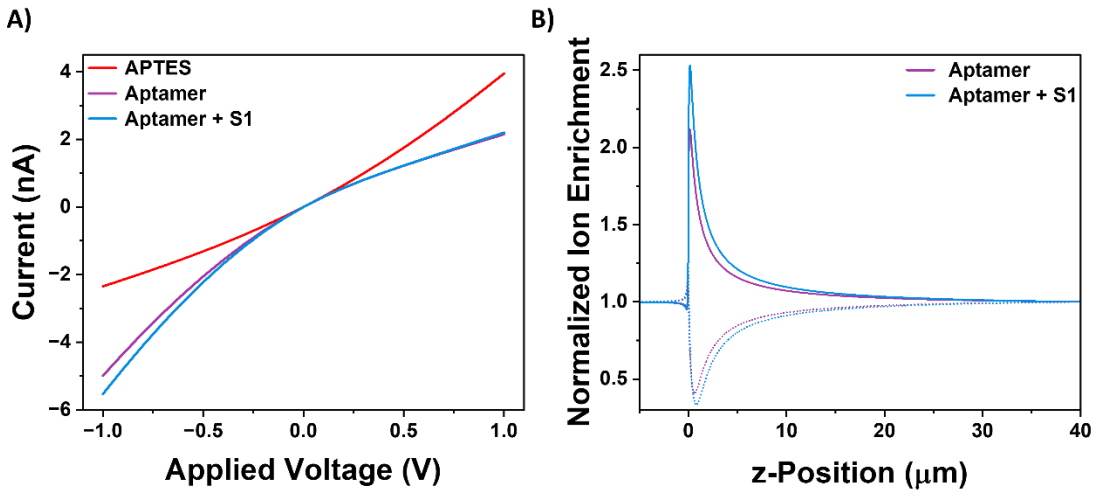

Figure S6: Simulated I-V curves of a quartz nanopipette modified with APTES, aptamer, and spike protein subunit on the surface. (B) The change in ionic enrichment of the aptamer state before (purple) and after (blue) the spike protein was binding. Solid lines are at -1 V applied potential, and dotted lines are at +1 V applied potential. The z-position represents the position along the central axisymmetric axis of the nanopore, with 0 representing the pore mouth and negative values representing the interior of the pore.

To qualitatively describe the response of the nanopore sensor upon the binding of varying concentrations of the S1 subunit, the spike surface density can be swept from 0 to the aptamer surface density (as each aptamer is assumed only to be able to accommodate one S1 subunit) (**Fig. S7**). The immobilization of the negatively charged spike protein subunit makes the surface charge density of the nanopipette more negative, increasing its rectification ratio. Although the magnitude of the change could not be replicated, the qualitative direction of change demonstrates that the immobilization of the negatively charged spike protein subunit alters the rectification ratio in the experimentally observed manner.

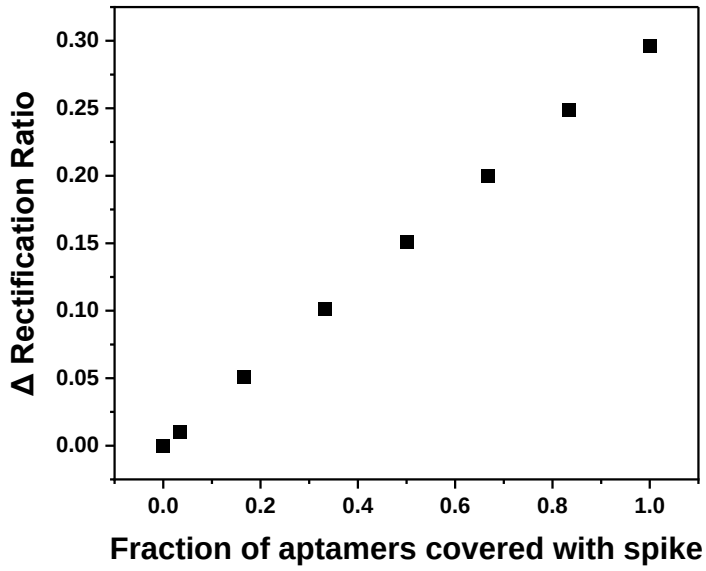

Figure S7: Finite Element Analysis of the change in the rectification ratio as the aptamers (3×10^{11} cm^{-2} surface density) are filled up with the negatively charged spike protein subunits.

S5. Stability Study of Aptamer-functionalized Nanopipettes

A continuous voltammetric cycling experiment was carried out to assess the stability of the aptamer-functionalized nanopipettes before and after target binding, as summarized in Figure S8. The RR observed for the aptamer-functionalized nanopipette remained stable for 100 cycles with no discernible degradation in signal. Subsequent exposure of these pipettes to the spike protein target resulted in increased rectification as initially observed, indicating the stability of the surface chemistry. The target-bound aptamer-functionalized nanopipettes were also subjected to continuous voltammetric cycling. The RR response observed was also stable for 100 cycles with minor fluctuations, indicating the stability of the aptamer-spike protein response. Attempts were made to investigate the reusability of the sensor through deionized water (stringency) washing and heating, but the probe-analyte binding could not be reversed. The developed aptamer-functionalized nanopore sensor, therefore, demonstrates high stability as a single-use device for viral fragment detection.

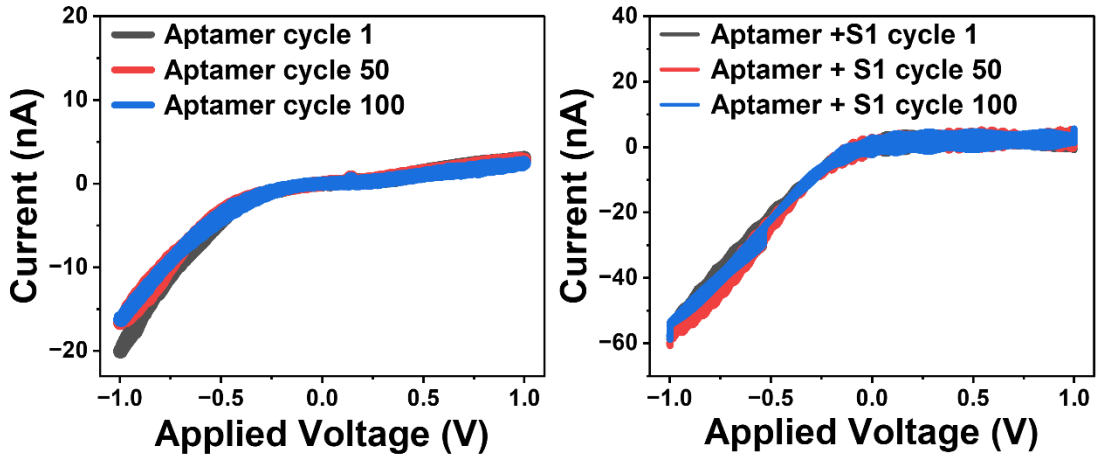

Figure S8: Sample I-V curves for the change in rectification ratio as a function of repeated voltammetric cycles in 10 mM KCl. Each cycle is iterated in minute intervals, rendering the x-axis proportional to time. Error bars are the standard error from the measurement of three unique devices.

Supplementary References

(1) Cao, C.; Cai, Z.; Xiao, X.; Rao, J.; Chen, J.; Hu, N.; Yang, M.; Xing, X.; Wang, Y.; Li, M.; et al. The architecture of the SARS-CoV-2 RNA genome inside virion. *Nature Communications* **2021**, *12* (1), 3917. DOI: 10.1038/s41467-021-22785-x.
(2) Bukkitgar, S. D.; Shetti, N. P.; Aminabhavi, T. M. Electrochemical investigations for COVID-19 detection-A comparison with other viral detection methods. *Chemical Engineering Journal* **2021**, *420*, 127575. DOI: 10.1016/j.cej.2020.127575.
(3) Giri, B.; Pandey, S.; Shrestha, R.; Pokharel, K.; Ligler, F. S.; Neupane, B. B. Review of analytical performance of COVID-19 detection methods. *Analytical and Bioanalytical Chemistry* **2021**, *413* (1), 35-48. DOI: 10.1007/s00216-020-02889-x.
(4) Udugama, B.; Kadhiresan, P.; Kozlowski, H. N.; Malekjahani, A.; Osborne, M.; Li, V. Y. C.; Chen, H.; Mubareka, S.; Gubbay, J. B.; Chan, W. C. W. Diagnosing COVID-19: The Disease and Tools for Detection. *ACS Nano* **2020**, *14* (4), 3822-3835. DOI: 10.1021/acsnano.0c02624.
(5) Zhang, S.; Li, M.; Su, B.; Shao, Y. Fabrication and Use of Nanopipettes in Chemical Analysis. *Annual Review of Analytical Chemistry* **2018**, *11* (1), 265-286. DOI: 10.1146/annurev-anchem-061417-125840.
(6) Farrell, E. B.; Duleba, D.; Johnson, R. P. Aprotic Solvent Accumulation Amplifies Ion Current Rectification in Conical Nanopores. *The Journal of Physical Chemistry B* **2022**, *126* (30), 5689-5694. DOI: 10.1021/acs.jpcb.2c03172.
(7) Lasserre, P.; Balansethupathy, B.; Vezza, V. J.; Butterworth, A.; Macdonald, A.; Blair, E. O.; McAteer, L.; Hannah, S.; Ward, A. C.; Hoskisson, P. A.; et al. SARS-CoV-2 Aptasensors Based on Electrochemical Impedance Spectroscopy and Low-Cost Gold Electrode Substrates. *Anal. Chem.* **2022**, *94* (4), 2126-2133. DOI: 10.1021/acs.analchem.1c04456.
(8) Etienne, E. E.; Nunna, B. B.; Talukder, N.; Wang, Y.; Lee, E. S. COVID-19 Biomarkers and Advanced Sensing Technologies for Point-of-Care (POC) Diagnosis. *Bioengineering (Basel)* **2021**, *8* (7). DOI: 10.3390/bioengineering8070098.
(9) Han, Y.; Mayer, D.; Offenhäusser, A.; Ingebrandt, S. Surface activation of thin silicon oxides by wet cleaning and silanization. *Thin Solid Films* **2006**, *510* (1), 175-180. DOI: 10.1016/j.tsf.2005.11.048.
(10) White, R. J.; Phares, N.; Lubin, A. A.; Xiao, Y.; Plaxco, K. W. Optimization of Electrochemical Aptamer-Based Sensors via Optimization of Probe Packing Density and Surface Chemistry. *Langmuir* **2008**, *24* (18), 10513-10518. DOI: 10.1021/la800801v.
(11) Piotr, P. Additional Positive Electric Residues in the Crucial Spike Glycoprotein S Regions of the New SARS-CoV-2 Variants. *Infection and Drug Resistance* **2021**, *14*, 5099-5105. DOI: 10.2147/IDR.S342068.